ADVANCED SCIENCE Open Access
www.advancedscience.com

MnO_2 Nanowires with Sub-10 nm Thick Conjugated Microporous Polymers as Synergistic Triboelectric Materials

Hanbyeol Jung, Dong-Min Lee, Jina Park, Taeho Kim, Sang-Woo Kim, and Seung Uk Son**

MnO_2 nanowires coated with conjugated microporous polymers (CMP) are applied as triboelectric energy harvesting materials. The tribopositive performance of the CMP shells is enhanced with the assistance of MnO_2 nanowires (MnO_2 NW), likely due to cationic charge transfer from the tribopositive CMP layers to the surface Mn^{2+} and Mn^{3+} species of MnO_2 NW. This is supported by model studies. The MnO_2@CMP-2 with sub-10 nm thick CMP layers shows promising triboelectric output voltages up to 576 V and a maximum power density of 1.31 mW cm^{-2}. Spring-assisted triboelectric nanogenerators fabricated with MnO_2@CMP-2/PVP-3 films are used as power supplies to operate electronic devices.

1. Introduction

Over the past decade, research on small-scale energy harvesting and utilization has gained considerable significance.[1] For instance, triboelectric energy in everyday life can be harvested and utilized for various purposes.[2] Since the Wang group developed triboelectric nanogenerators (TENGs),[3] extensive research has focused on fabricating new devices.[4] In addition, to improve the efficiency of TENGs, extensive studies have been conducted on triboelectric materials.[5]

As triboelectric energy harvesting materials, various organic polymers have been studied.[6] In addition, the surface areas and electronic properties of polymers have been tuned to enhance their triboelectric performance.[7–9] For example, microporous organic materials with high surface areas have been studied for engineering TENGs.[7,8] As a class of microporous organic materials, conjugated microporous polymers (CMPs) have been prepared by the coupling of organic building blocks.[10] Recently, our research group reported that CMPs can be used as promising tribopositive materials for harvesting triboelectric energy.[11]

On the other hand, porous organic polymer-inorganic composites have been studied to achieve enhanced triboelectric performance.[12] The triboelectrification performance of organic polymers can be enhanced with the assistance of inorganic nanomaterials. While organic polymer materials offer advantages in facile chemical engineering, inorganic nanomaterials can provide additional benefits such as facilitating redox reactions.

Recently, MnO_2 nanomaterials have been utilized as energy storage materials in pseudocapacitors.[13] The morphology of MnO_2-based nanomaterials has been engineered into nanowires. Usually, the surface of MnO_2 nanowires has an amorphous character and consists of Mn^{2+} and Mn^{3+} species,[14] which can be further oxidized to Mn^{4+} species by donating electrons.

It can be speculated that core–shell MnO_2@CMP nanowires can be engineered to enhance the tribopositive performance of CMP materials with the assistance of surface Mn^{2+} and Mn^{3+} species in the inner MnO_2 nanowires. When preparing MnO_2@CMP nanowires, we observed the facile generation of static electricity in a Falcon plastic tube (Figure S1 and Movie S1, Supporting Information). In this work, we report the preparation of MnO_2@CMP nanowires and their enhanced triboelectric performance, compared to the corresponding MnO_2 and CMP materials.

2. Results and Discussion

Figure 1 displays the synthetic scheme of MnO_2@CMP nanowires.

First, MnO_2 nanowires (MnO_2 NW) were prepared by reacting $KMnO_4$ with H_2O_2 in acetic acid.[15] Through the Sonogashira coupling of 1,3,5-triethynylbenzene with 1.5 eq. 1,4-diiodobenzene in the presence of MnO_2 NW, CMP layers were formed on the MnO_2 NW. With a fixed amount of MnO_2 NW (0.20 g), the amount of 1,3,5-triethynylbenzene was gradually

H. Jung, J. Park, T. Kim, S. U. Son
Department of Chemistry
Sungkyunkwan University
Suwon 16419, South Korea
E-mail: sson@skku.edu
D.-M. Lee, S.-W. Kim
Department of Materials Science and Engineering
Yonsei University
Seoul 03722, South Korea
E-mail: kimsw1@yonsei.ac.kr
D.-M. Lee, S.-W. Kim
Center for Human-Oriented Triboelectric Energy Harvesting
Yonsei University
Seoul 03722, South Korea

The ORCID identification number(s) for the author(s) of this article can be found under https://doi.org/10.1002/advs.202409917

DOI: 10.1002/advs.202409917

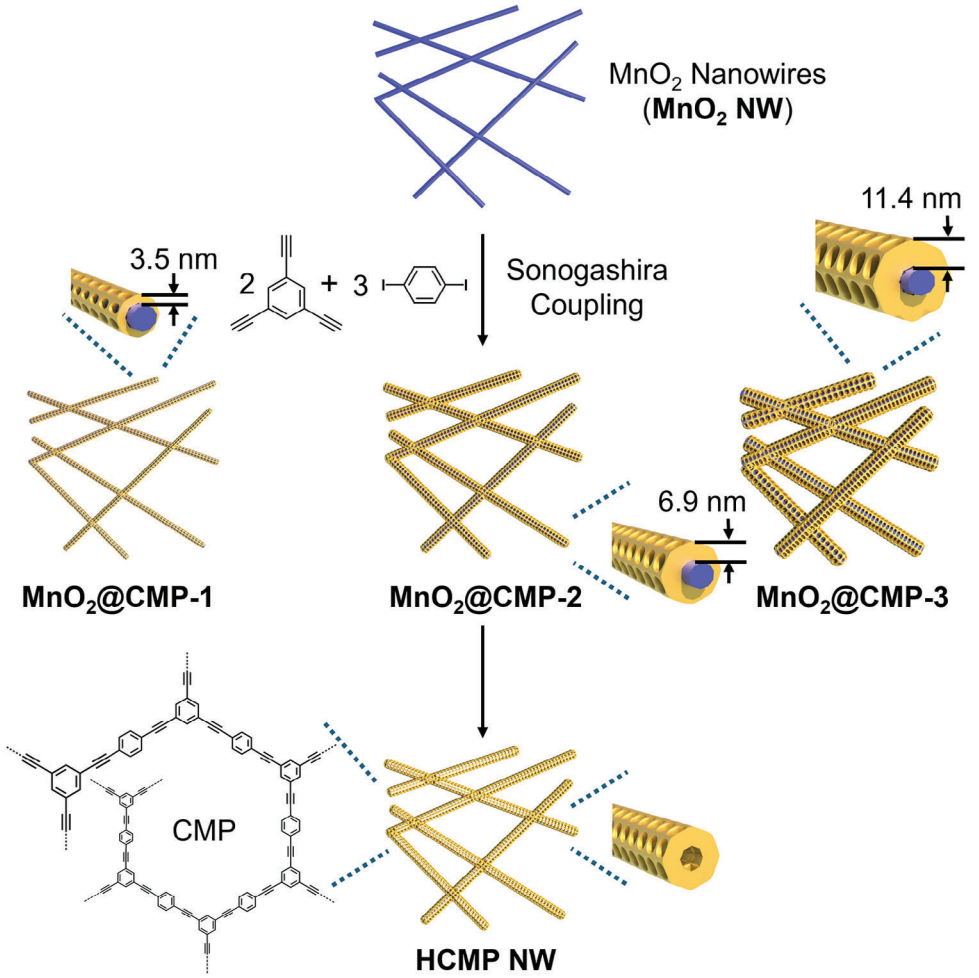

Figure 1. Synthesis of MnO_2@CMP nanowires and HCMP nanowires (HCMP NW).

increased from 0.10 to 0.20 and 0.40 mmol to form three different MnO_2@CMP nanowires (denoted as MnO_2@CMP-1, MnO_2@CMP-2, and MnO_2@CMP-3, respectively). As control materials, the inner MnO_2 of MnO_2@CMP-2 was etched by treating with HCl to form hollow CMP nanowires (HCMP NW).

The morphologies of materials were examined using scanning (SEM) and transmission electron microscopy (TEM) (**Figure 2**). The SEM and TEM images of MnO_2 NW revealed long nanowires with a thickness of 15–25 nm and a length of 2–5 µm (Figure 2a–c). While MnO_2@CMPs retained wire-like morphologies (Figure 2d,e,g,h,j,k), a closer inspection revealed a thin coating of CMP on the surface of MnO_2 NW (Figure 2f,i,l). The coating thicknesses of CMPs in MnO_2@CMP-1, MnO_2@CMP-2, and MnO_2@CMP-3 were measured to be 3.5 ± 0.4, 6.9 ± 0.7, and 11.4 ± 0.7 nm, respectively (Figure S2, Supporting Information). Whilst the SEM images of HCMP NW showed wire-like morphologies, the empty inner space could be confirmed by TEM analysis (Figure 2m–o).

The chemical and physical features of materials were investigated using various analytical techniques (**Figure 3**). Powder X-ray diffraction (PXRD) studies on MnO_2 NW and MnO_2@CMPs showed diffraction peaks at 12.5°, 17.9°, 28.6°, 37.5°, 41.6°, 50.0°, 60.3°, and 69.6°, corresponding to the (110), (200), (310), (211), (301), (411), (521), and (541) crystalline planes of α-MnO_2 (JCPDS# 44–141) (Figure 3a).[16] In comparison, HCMP NW exhibited an amorphous feature, which is a conventional characteristic of CMPs in the literature.[17]

N_2 sorption studies were conducted to investigate the surface areas and porosity of materials (Figure 3b). The analysis of N_2 sorption isotherm curves based on the Brunauer–Emmett–Teller (BET) theory indicated that the MnO_2 NW has a surface area of 54 $m^2\ g^{-1}$ and poor porosity. In comparison, the HCMP NW showed a high surface area of 310 $m^2\ g^{-1}$ and microporosity (pore sizes < 2 nm) with a total pore volume (V_t) of 0.46 $cm^3\ g^{-1}$. As the amount of CMPs increased in the MnO_2@CMPs, the surface areas gradually increased from 85 $m^2\ g^{-1}$ (MnO_2@CMP-1) to 138 (MnO_2@CMP-2) and 207 $m^2\ g^{-1}$ (MnO_2@CMP-3) with the increase of V_t from 0.11 $cm^3\ g^{-1}$ to 0.12 and 0.13 $cm^3\ g^{-1}$, respectively.

The infrared (IR) absorption spectra of MnO_2 NW and MnO_2@CMPs revealed broad peaks at 460–520 cm^{-1}, corresponding to Mn—O vibrations (Figure 3c).[18] In comparison, HCMP NW showed aromatic C=C and C—H vibration peaks at 1581 and 837 cm^{-1}, respectively, in addition to the C—O vibration

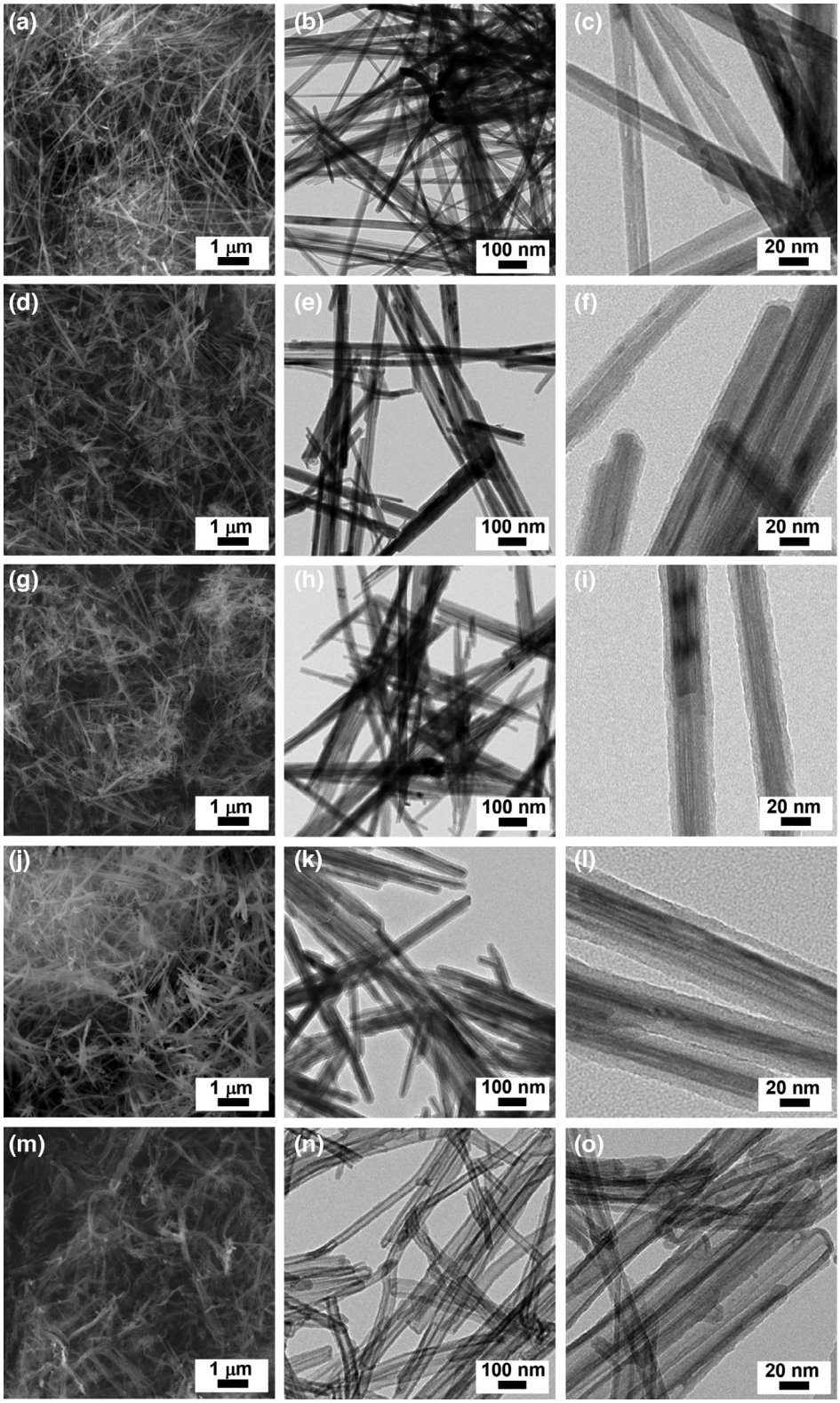

Figure 2. SEM and TEM images of (a,b,c) MnO_2 NW, (d,e,f) MnO_2@CMP-1, (g,h,i) MnO_2@CMP-2, (j,k,l) MnO_2@CMP-3, and (m,n,o) HCMP NW.

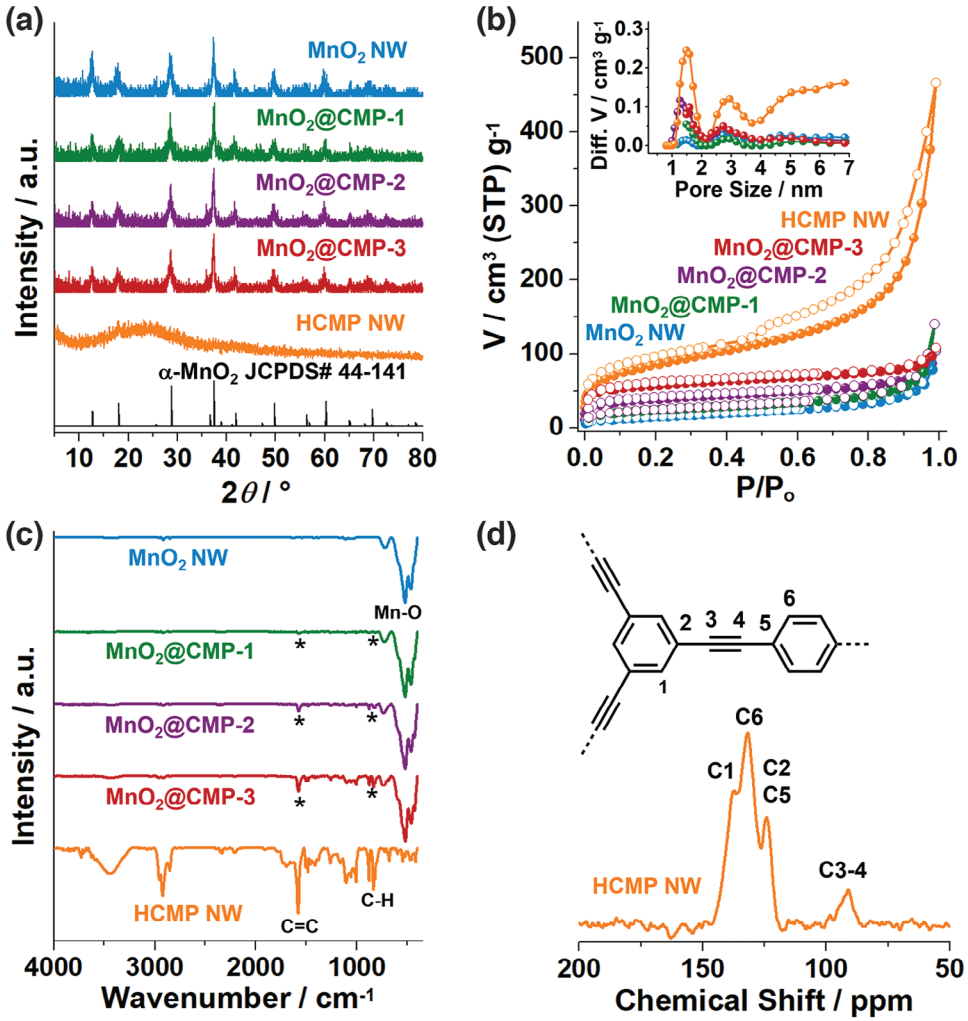

Figure 3. a) PXRD patterns, b) N_2 adsorption–desorption isotherm curves obtained at 77 K and pore size distribution diagrams based on the NL-DFT method, c) IR spectra of MnO_2 NW, MnO_2@CMPs, and HCMP NW. d) A solid-state ^{13}C NMR spectrum of HCMP NW.

at 1010–1105 cm^{-1}, which was generated through the oxidation of CMP by MnO_2 at the interfaces.[19] As expected, as the amount of CMP increased in MnO_2@CMPs, the corresponding vibration peaks of CMPs gradually increased (indicated by asterisks in Figure 3c). A solid-state ^{13}C nuclear magnetic resonance (NMR) spectrum of HCMP NW exhibited alkyne and aromatic carbon peaks at 91 and 124–138 ppm, respectively, consistent with the CMPs reported in the literature (Figure 3d).[20]

The high-resolution (HR)-TEM analysis of MnO_2 NW and MnO_2@CMP-2 showed a crystalline inner part showing the (200) crystal plane of α-MnO_2 with an interlayer distance of 0.49 nm (**Figure** 4a,b).[21] The surface (a depth of ≈1.8 nm) of MnO_2 NW displayed amorphous and defective features (indicated by dotted lines in Figure 4a,b). The MnO_2@CMP-2 showed the additional coating of amorphous CMP materials on the MnO_2 NW (Figure 4b).

Energy dispersive X-ray spectroscopy (EDS)-based elemental mapping studies of MnO_2 NW showed homogeneous distributions of Mn and O elements (Figure 4c). In comparison, MnO_2@CMP-2 showed a homogeneous distribution of carbon elements on the surface of MnO_2 NW, indicating a successful coating of CMP (Figure 4d).

The chemical surroundings of materials were investigated by X-ray photoelectron spectroscopy (XPS). The XPS Mn $2p_{3/2}$ and $2p_{1/2}$ orbital peaks of MnO_2 NW and MnO_2@CMPs were analyzed into three sets (Figure 4e; Figures S3 and S4, Supporting Information). Whilst the Mn $2p_{3/2}$ and $2p_{1/2}$ orbital peaks of Mn^{2+} species appeared at 641.0 and 652.7 eV, respectively, those of Mn^{3+} species appeared at 641.8 and 653.5 eV, respectively.[22] In comparison, those of Mn^{4+} species were observed at 643.7 and 655.4 eV, respectively.[22] The ratios of $Mn^{4+}/(Mn^{2+}+Mn^{3+})$ of MnO_2 NW, MnO_2@CMP-1, MnO_2@CMP-2, and MnO_2@CMP-3 were analyzed to be 0.31, 0.38, 0.42, and 0.44, respectively. These observations indicate that the surface of MnO_2 NW consists of defective Mn^{2+} and Mn^{3+} species. The O 1s orbital spectrum of MnO_2 NW showed two peaks at 529.3 and 530.3 eV, corresponding to the Mn—O—Mn and Mn—OH species, respectively (Figure 4f; Figures S3 and S5, Supporting Information).[23] The O 1s orbital spectra of MnO_2@CMPs and HCMP NW showed additional peaks at 531.9 and 533.2 eV, corresponding to C—O

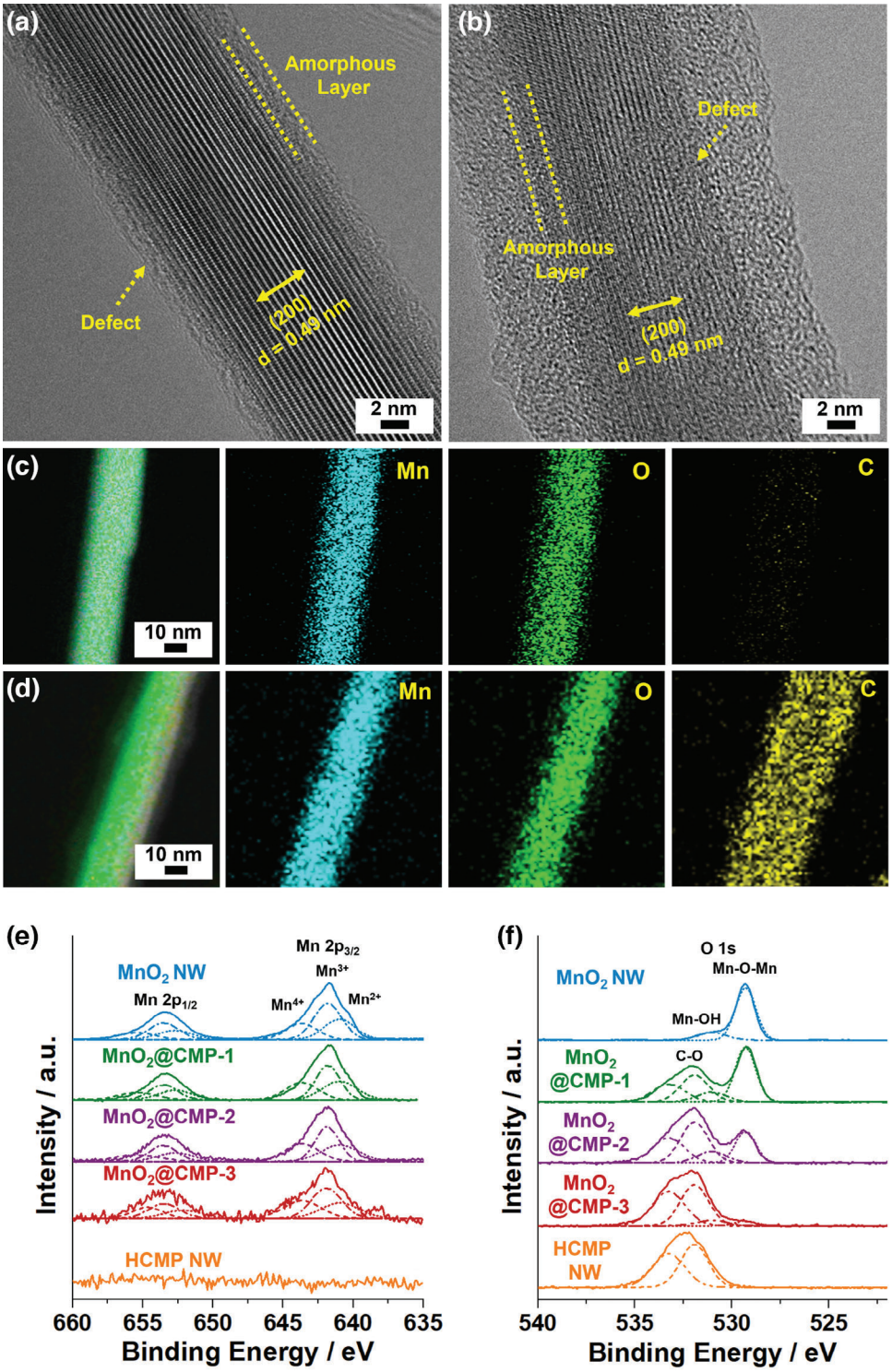

Figure 4. HR-TEM images of a) MnO_2 NW and b) MnO_2@CMP-2. EDS elemental mapping images of c) MnO_2 NW and d) MnO_2@CMP-2. e,f) XPS Mn 2p and O 1s orbital peaks of MnO_2 NW, MnO_2@CMPs, and HCMP NW with normalized intensities (Refer to Figure S3, Supporting Information for unnormalized ones).

species that were generated through oxidation of CMP by MnO_2 at the interfaces.[24]

To study triboelectric performance, the films of materials were fabricated using polyvinylpyrrolidone (PVP) as a matrix (**Figure 5a** and refer to Experimental Section in the Supporting Information). First, five MnO_2 NW/PVP films containing 1, 3, 5, 7, and 10 wt.% MnO_2 NW were fabricated (corresponding films were denoted as MnO_2 NW/PVP-1–5, respectively). As the amount of MnO_2 NW increased, the brown color of the films became more intense (Figure 5a). According to thermogravimetric analysis (TGA), the content of MnO_2 NW in MnO_2@CMP-2 was analyzed to be 72 wt.% (Figure S6, Supporting Information). Considering the information, five brown MnO_2@CMP-2/PVP films containing 1.4, 4.2, 6.9, 9.7, and 13.9 wt.% MnO_2@CMP-2 (corresponding to 1, 3, 5, 7, and 10 wt.% MnO_2 NW and 0.4, 1.2, 1.9, 2.7, and 3.9 wt.% CMP-2, respectively) were fabricated and denoted as MnO_2@CMP-2/PVP-1–5, respectively. In addition, five pale yellow HCMP NW/PVP films containing 0.4, 1.2, 1.9, 2.7, and 3.9 wt.% HCMP NW were fabricated and denoted as HCMP NW/PVP-1–5, respectively.

While the top view SEM images of MnO_2 NW/PVP-1–2, MnO_2@CMP-2/PVP-1–2, and HCMP NW/PVP-1–2 films exhibited flat surfaces, MnO_2 NW, MnO_2@CMP-2, and HCMP materials were detected in the MnO_2 NW/PVP-3–5, MnO_2@CMP-2/PVP-3–5, and HCMP NW/PVP-3–5 films (Figure S7, Supporting Information). The thicknesses of MnO_2 NW/PVP, MnO_2@CMP-2/PVP, and HCMP NW/PVP films were measured to be 25 μm (Figure S8, Supporting Information). The IR spectra of films showed exclusively the C—H, C═O, C—N, and C—O vibration peaks of the PVP matrix at 2891–2957, 1659, 1450, and 1283 cm^{-1}, respectively,[25] due to the relatively small amount of MnO_2 NW, MnO_2@CMP-2, and HCMP in the films (Figure S9, Supporting Information). While the PXRD patterns of MnO_2 NW/PVP-1, MnO_2@CMP-2/PVP-1, and HCMP NW/PVP-1–5 films showed broad diffraction peaks at 2θ of 10.3° and 20.7°, corresponding to the PVP matrix,[26] those of MnO_2 NW/PVP-2–5 and MnO_2@CMP-2/PVP-2–5 films revealed the original diffraction peaks of α-MnO_2 (Figure S10, Supporting Information).

The triboelectric performance of MnO_2 NW/PVP, MnO_2@CMP-2/PVP, and HCMP/PVP films with an area of 2 cm × 2 cm was studied (Figure 5b–e; Figure S11, Supporting Information). As a tribonegative material, perfluoroalkoxy alkanes (PFA) were used.[27] In the case of pristine PVP and MnO_2 NW/PVP films, as the amount of MnO_2 NW increased, the output peak-to-peak voltages ($V_{p\text{-}p}$) gradually increased from 234 V (PVP) to 302 (MnO_2 NW/PVP-1), 329 (MnO_2 NW/PVP-2), and 365 V (MnO_2 NW/PVP-3), respectively (Figure 5b). The corresponding output currents ($I_{p\text{-}p}$) increased from 16.8 μA (PVP) to 21.1 (MnO_2 NW/PVP-1), 24.3 (MnO_2 NW/PVP-2), and 26.0 μA (MnO_2 NW/PVP-3), respectively (Figure S11, Supporting Information). Then, the $V_{p\text{-}p}$ of MnO_2 NW/PVP-4 and MnO_2 NW/PVP-5 films decreased to 331 and 265 V, respectively, with a decrease of $I_{p\text{-}p}$ to 24.1 and 19.6 μA. In the case of HCMP NW/PVP films, as the amount of HCMP NW increased, $V_{p\text{-}p}$ gradually increased from 339 V (HCMP NW/PVP-1) to 385 (HCMP/PVP-2) and 456 V (HCMP/PVP-3) with an increase of $I_{p\text{-}p}$ from 23.8 to 25.9 and 31.7 μA (Figure 5c; Figure S11, Supporting Information). Then, the $V_{p\text{-}p}$ of HCMP NW/PVP-4 and HCMP NW/PVP-5 films decreased to 359 and 306 V, respectively, with a decrease of $I_{p\text{-}p}$ to 25.8 and 21.4 μA.

In comparison, as the amount of MnO_2@CMP-2 increased, $V_{p\text{-}p}$ significantly increased from 375 V (MnO_2@CMP-2/PVP-1) to 507 (MnO_2@CMP-2/PVP-2) and 576 V (MnO_2@CMP-2/PVP-3) with an increase of $I_{p\text{-}p}$ from 25.9 to 36.1 and 39.6 μA (Figure 5d; Figure S11, Supporting Information). Then, the $V_{p\text{-}p}$ of MnO_2@CMP-2/PVP-4 and MnO_2@CMP-2/PVP-5 films decreased to 359 and 306 V, respectively, with a decrease of $I_{p\text{-}p}$ to 36.1 and 24.4 μA. These observations indicated that the MnO_2 NW/PVP-3, HCMP NW/PVP-3, and MnO_2@CMP-2/PVP-3 are the best films. Among these films, the triboelectric performance was gradually enhanced in the order of MnO_2 NW/PVP-3 < HCMP NW/PVP-3 < MnO_2@CMP-2/PVP-3 (Figure 5e).

According to Kelvin probe force microscopy (KPFM), the surface potentials gradually increased from 341 mV (PVP) to 387 (MnO_2 NW/PVP-3), 446 (HCMP NW/PVP-3), and 520 mV (MnO_2@CMP-2/PVP-3), matching with the observed trend of the tribopositive performance of films (**Figure 6a**). The mechanism of electricity generation through triboelectrification has been reported in the literature (Figure 6b).[28] At the contact of the pressed two films, electrons transfer from the tribopositive MnO_2@CMP-2/PVP-3 film to the tribonegative PFA film. In the releasing state, electrons flow from the supporting metal electrode of a PFA film to the supporting metal electrode of an MnO_2@CMP-2/PVP-3 film, reaching an equilibrium state. During the re-pushing state of two films, electrons flow back from the supporting metal electrode of an MnO_2@CMP-2/PVP-3 film to the supporting metal electrode of a PFA film. This process was repeated in the pushing/releasing cycles.

We propose the following mechanistic principle for the enhanced tribopositive performance of MnO_2@CMP-2 (Figure 6c). When the PFA film is in contact with MnO_2@CMP-2, electrons transfer from the tribopositive CMP to the PFA. The surface Mn^{2+} (indicated as red balls in Figure 6c) and Mn^{3+} (indicated as orange balls in Figure 6c) species can be converted to Mn^{4+} (indicated as blue balls in Figure 6c) through electron transfer to the CMP layers. With the assistance of the surface Mn^{2+} and Mn^{3+} species in MnO_2 NW, the CMP layers can further enhance their role as tribopositive materials.

To investigate the possible redox behaviors of the surface Mn^{2+} and Mn^{3+} species of MnO_2 NW, we conducted the following model studies (**Figure 7**; Figures S12–S14, Supporting Information). Because PFA is a polymeric material and the generation of cationic charges on CMP through triboelectrification is an instantaneous event, XPS studies on the changes of the surface Mn^{2+} and Mn^{3+} species of MnO_2 NW are technically limited. Thus, we treated MnO_2 NW with tetracyanoquinone (TCNQ), as an electron-deficient model compound,[29] and trityl tetrafluoroborate ($TritylBF_4$),[30] as a model carbocation (Figure 7a).

When the MnO_2 NW was treated with TCNQ and $TritylBF_4$, the XPS Mn 2p orbital peaks significantly shifted to the higher energy region by 0.21 and 0.35 eV, respectively, indicating the conversion of the surface Mn^{2+} and Mn^{3+} species to Mn^{3+} and Mn^{4+} species. The detailed analysis indicated an increase in the $Mn^{4+}/(Mn^{2+} + Mn^{3+})$ values from 0.31 to 0.42 and 0.43 after the treatment of the MnO_2 NW with TCNQ and $TritylBF_4$, respectively (Figure 7b; Figure S12, Supporting Information).

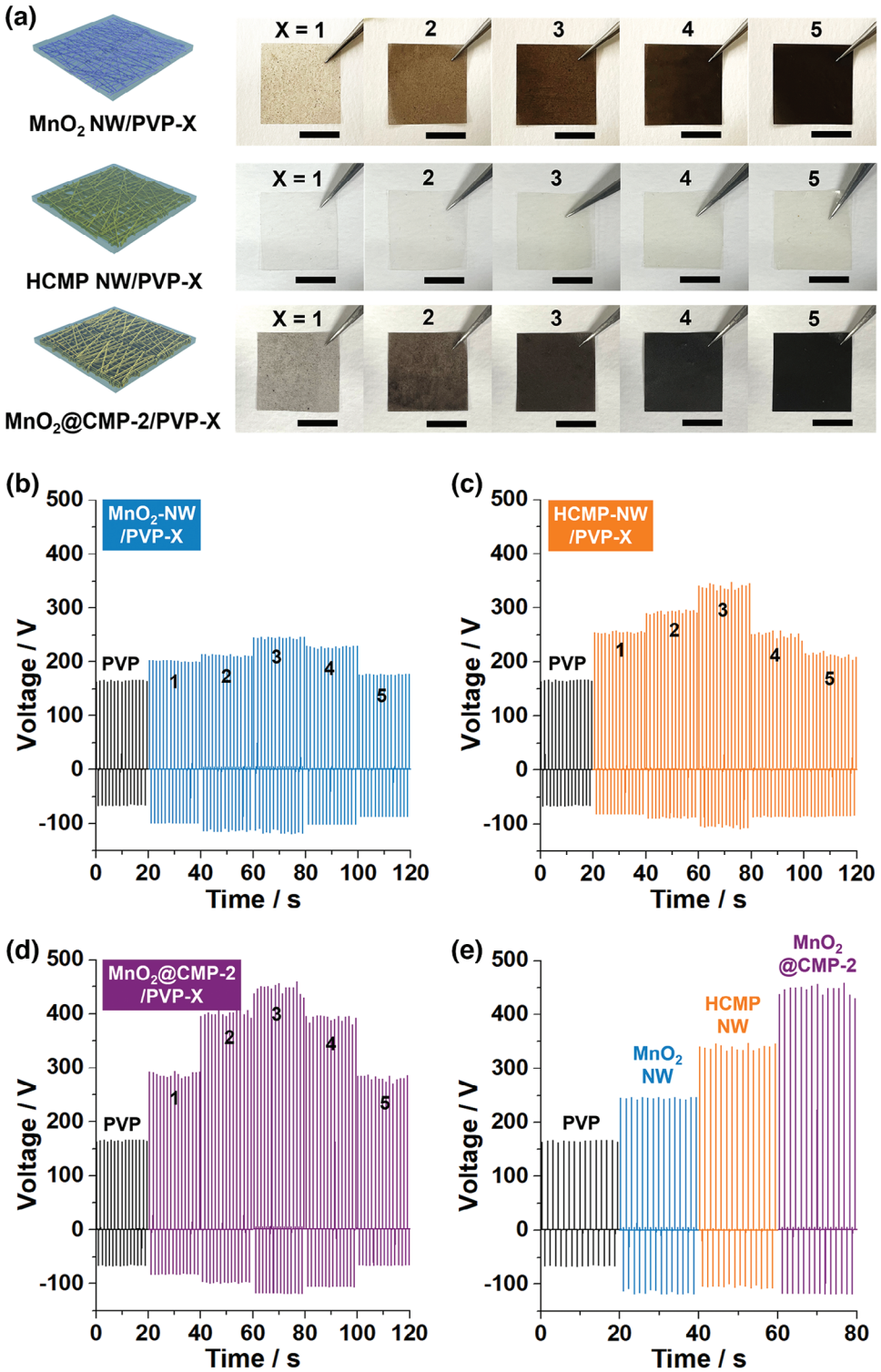

Figure 5. a) Photographs of MnO_2 NW/PVP-1–5, HCMP NW/PVP-1–5, and MnO_2@CMP-2/PVP-1–5 films (scale bars: 1 cm). Triboelectric output voltages of b) MnO_2 NW/PVP-1–5, c) HCMP NW/PVP-1–5, d) MnO_2@CMP-2/PVP-1–5 films. e) Comparative display of the output voltages of PVP, MnO_2 NW/PVP-3, MnO_2@CMP-2/PVP-3, and HCMP NW/PVP-3 films (a working area of 2 cm × 2 cm, pushing force of 2 kgf, pushing frequency of 0.73 Hz, RH 50%, PFA as a tribonegative material. Refer to Figure S11 (Supporting Information) for the output currents of corresponding films.

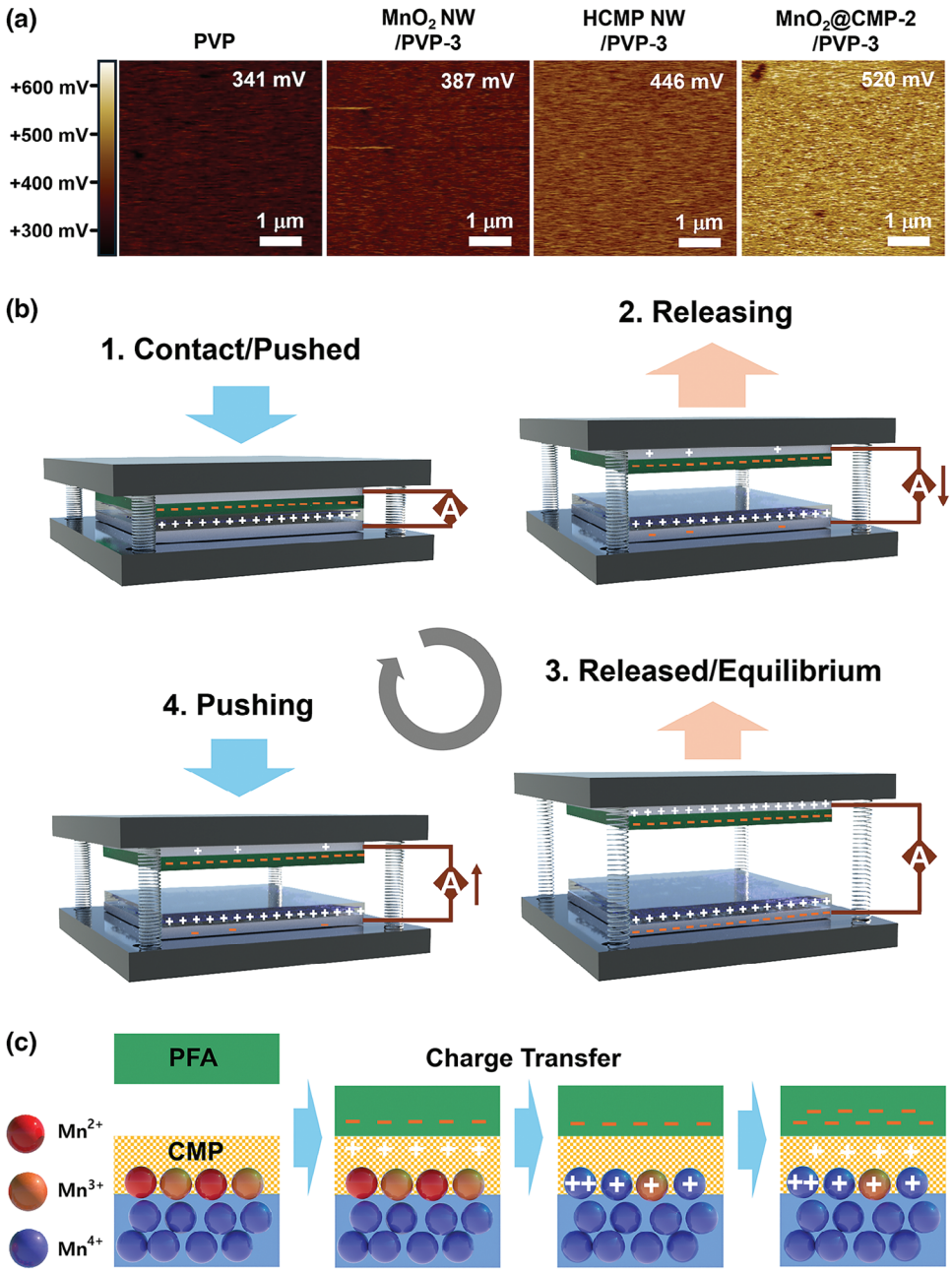

Figure 6. a) KPFM images of PVP, MnO_2 NW/PVP-3, HCMP NW/PVP-3, and MnO_2@CMP-2/PVP-3 films. b) A mechanism of the triboelectric energy harvesting process by a tribopositive a MnO_2@CMP-2/PVP film and a tribonegative PFA film. c) A suggested mechanism of the MnO_2 NW-assisted tribopositive performance of MnO_2@CMP-2.

In addition, the O 1s orbital peaks of Mn—O—Mn species also shifted to the higher energy region by 0.18 and 0.32 eV, respectively, indicating the increased oxidation state of Mn species (Figure 7c; Figure S13, Supporting Information). Electron paramagnetic resonance (EPR) spectra confirmed the generation of anionic TCNQ radicals and trityl radicals (Figure S14, Supporting Information). These observations indicate that the surface Mn^{2+} and Mn^{3+} species of MnO_2 NW can be converted to Mn^{3+} and Mn^{4+} species through the interaction with electron-deficient materials and carbocation species.

The thickness effect of CMP layers on the triboelectric performance of MnO_2@CMPs was investigated (**Figure** 8a,b; Figure S15, Supporting Information). The MnO_2@CMP-1 with 3.5 ± 0.4 nm thick CMP layers showed slightly better triboelectric performance with $V_{p\text{-}p}$ of 590 V and $I_{p\text{-}p}$ of 40.8 μA than the MnO_2@CMP-2 with 6.9 ± 0.7 nm thick CMP layers displaying $V_{p\text{-}p}$ of 576 V and $I_{p\text{-}p}$ of 39.6 μA. In comparison, the MnO_2@CMP-3 with 11.4 ± 0.7 nm thick CMP layers showed significantly lower $V_{p\text{-}p}$ of 505 V and $I_{p\text{-}p}$ of 34.2 μA. These results indicate that the thickness of CMP layers should be sufficiently

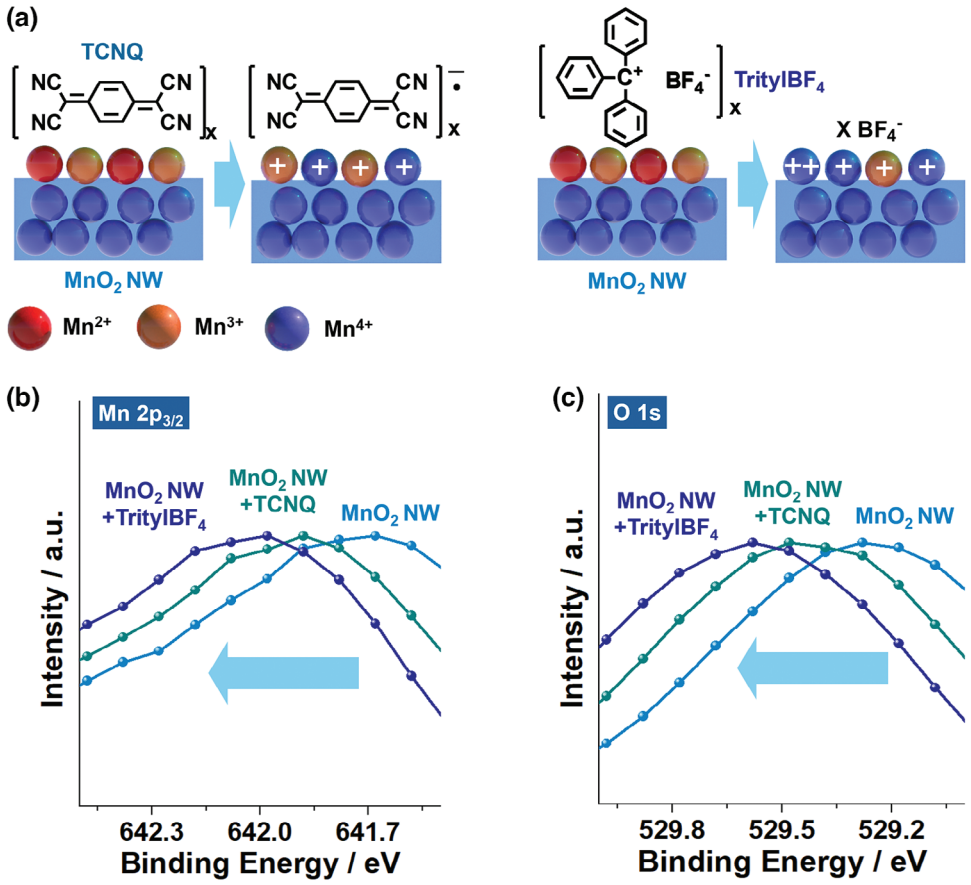

Figure 7. a) Model reactions of MnO_2 NW with tetracyanoquinone (TCNQ) and trityl tetrafluoroborate ($TritylBF_4$). XPS b) Mn $2p_{3/2}$ and c) O 1s orbital spectra of MnO_2 NW with normalized intensities before and after treatment of MnO_2 NW with TCNQ and $TritylBF_4$ (Refer to Figures S12 and S13, Supporting Information for detailed analysis).

thin at a sub-10 nm scale for efficient charge transfer to the inner MnO_2 NW during the triboelectrification process.

The working condition-dependent triboelectric performance of the MnO_2@CMP-2/PVP-3 was investigated (Figure 8c,d; Figures S16 and S17, Supporting Information). At relative humidities (RH) of 30% and 50%, the MnO_2@CMP-2/PVP-3 exhibited similar triboelectric performance with $V_{p\text{-}p}$ of 554 and 576 V, respectively, and $I_{p\text{-}p}$ of 39.2 and 39.6 μA, respectively (Figure S16, Supporting Information). When RH increased to 80%, the $V_{p\text{-}p}$ and $I_{p\text{-}p}$ significantly dropped to 310 V and 28.7 μA, respectively.

The triboelectric performance of MnO_2@CMP-2/PVP-3 was sensitive to the pushing force (Figure 8c; Figure S17, Supporting Information). As the pushing forces increased from 0.5 to 1, 1.5, 2, and 2.5 kgf, the $V_{p\text{-}p}$ increased from 322 to 363, 431, 576, and 600 V, respectively, with an increase of $I_{p\text{-}p}$ from 22.5 to 24.6, 30.3, 39.6, and 42.0 μA. In contrast, the MnO_2@CMP-2/PVP-3 exhibited similar triboelectric performance across a pushing frequency range of 0.23–2.57 Hz, maintaining $V_{p\text{-}p}$ of 575–576 V and $I_{p\text{-}p}$ of 39.6–39.8 μA (Figure 8d; Figure S17, Supporting Information).

The durability of MnO_2@CMP-2/PVP-3 was studied through cycling tests (Figure 8e). At the optimized working conditions (a pushing force of 2 kgf, a pushing frequency of 0.73 Hz, RH 50%), the MnO_2@CMP-2/PVP-3 maintained the original triboelectric performance in the range of 98.8–100% over 21 000 cycling tests.

Resistance-dependent current and power densities generated by triboelectric MnO_2@CMP-2/PVP-3 films were measured, showing a maximum power density (P_{max}) of 1.31 mW cm^{-2} at a resistance of 5×10^7 Ω (**Figure 9a**). Very recently, microporous organic materials such as covalent organic frameworks (COFs) and CMPs have been applied as triboelectric materials, showing $V_{p\text{-}p}$ of 40–815 V and P_{max} of 0.364 μW cm^{-2}–0.824 mW cm^{-2} (Table S1, Supporting Information).[8,11] In addition, metal–organic framework (MOF)-based triboelectric materials showed the $V_{p\text{-}p}$ of 62–658 V and P_{max} of 0.968 μW cm^{-2}–0.508 mW cm^{-2} (Table S2, Supporting Information).[9] In this regard, the triboelectric performance of the MnO_2@CMP-2/PVP-3 film, showing $V_{p\text{-}p}$ of 576 V and P_{max} up to 1.31 mW cm^{-2}, is quite promising.

The triboelectric MnO_2@CMP-2/PVP-3 film could be utilized to charge electrolytic capacitors (Figure 9b). After 5 min, voltages of 50, 32, 15, and 5 V were achieved for 4.7, 10, 33, and 100 μF capacitors, respectively. Spring-assisted triboelectric nanogenerators (S-TENGs) were fabricated using MnO_2@CMP-2/PVP-3 and PFA films (Figure 9c,d). It was confirmed that the S-TENG could work as a power supply to illuminate 100 green LED bulbs (Figure 9e; Movie S2, Supporting Information). Moreover, after a battery was removed from an electronic calculator, the S-TENG was connected as a power supply. A capacitor charged to 6 V for

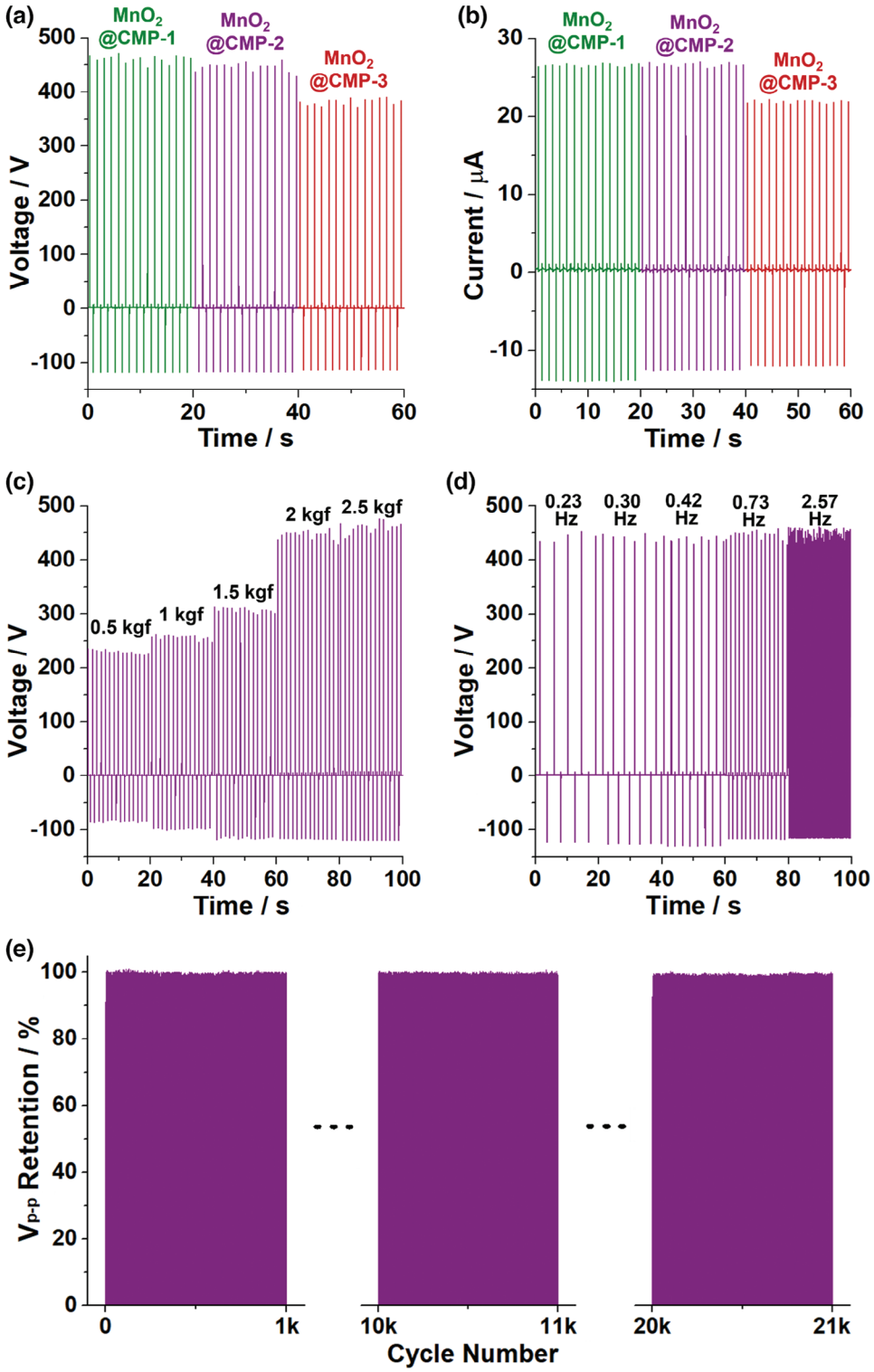

Figure 8. a,b) CMP layers thickness-dependent output voltages and currents of MnO_2@CMP/PVP films (Refer to Figure S15, Supporting Information for more studies). c) Pushing force and d) pushing frequency-dependent output voltages and e) the retention of output voltages of MnO_2@CMP-2/PVP-3 film (standard working conditions: a working area of 2 cm × 2 cm, a pushing force of 2 kgf, a pushing frequency of 0.73 Hz, RH 50%). Refer to Figures S16 and S17, Supporting Information for the output currents of corresponding films.

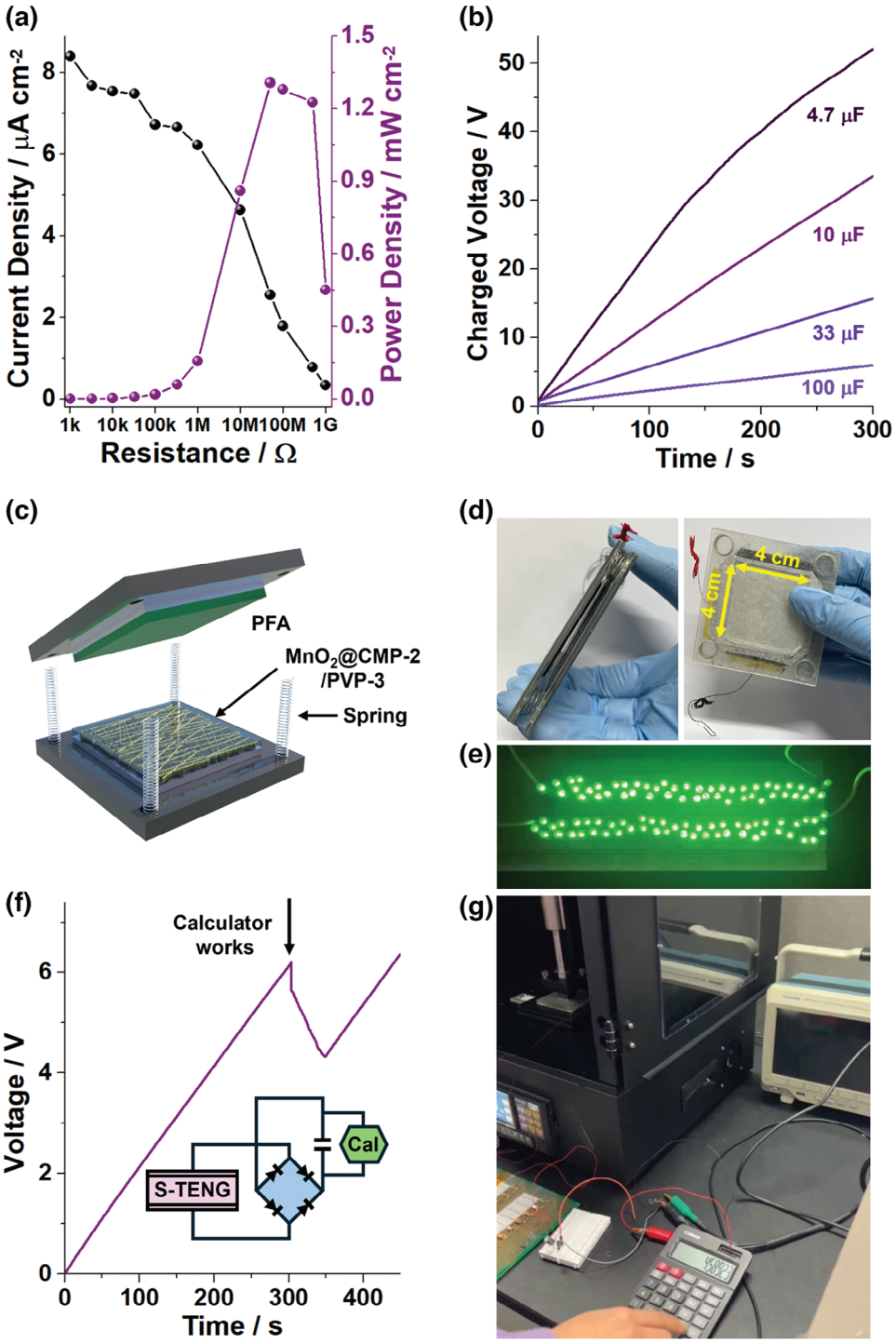

Figure 9. a) Resistance-dependent current and power densities (a film area of 2 cm × 2 cm, a pushing force of 2 kgf) and b) charged voltages of electrolytic capacitors by the triboelectric performance of a MnO_2@CMP-2/PVP-3 film. c) An illustration and d) a photograph of an S-TENG fabricated using MnO_2@CMP-2/PVP-3 and PFA films. e,f,g) Demonstration of S-TENGs as power sources to turn on 100 green LED bulbs and to operate an electronic calculator (working conditions: a film area of 4 cm × 4 cm, a pushing force of 2 kgf, a pushing frequency of 0.73 Hz, RH 50%).

300 s using the S-TENG could be used to operate a calculator (Figure 9f,g; Movie S3, Supporting Information).

3. Conclusion

In conclusion, this work shows that the triboelectric performance of CMP materials can be significantly enhanced with the assistance of MnO_2 NW. As a cooperative mechanistic principle for the triboelectrification of MnO_2@CMP, the possible redox role of the surface Mn^{2+} and Mn^{3+} species of MnO_2 NW was suggested. Especially, the CMP shell thickness of MnO_2@CMP was also critical and should be a sub-10 nm scale to ensure efficient tribopositive materials. Model studies supported the possible electron transfer from the surface Mn^{2+} and Mn^{3+} species of MnO_2 NW to organic materials. Based on the observed results of this work, we believe that various redox-active inorganic material@CMP systems can be developed as effective triboelectric materials.

Supporting Information

Supporting Information is available from the Wiley Online Library or from the author.

Acknowledgements

H.J. and D.M.L. contributed equally to this work. This work was supported by the National Research Foundation of Korea (NRF) grant (Nos. RS-2023-00208797 and 2022R1A3B1078291) funded by the Korean government (MSIT).

Conflict of Interest

The authors declare no conflict of interest.

Data Availability Statement

The data that support the findings of this study are available in the supplementary material of this article.

Keywords

conjugated microporous polymer, manganese dioxide, nanowire, triboelectric material, triboelectric nanogenerator

Received: August 19, 2024
Revised: September 24, 2024
Published online: November 3, 2024

[1] Z. L. Wang, *MRS Bull.* **2023**, *48*, 1014.
[2] T. Cheng, J. Shao, Z. L. Wang, *Nat. Rev. Methods Primers* **2023**, *3*, 39.
[3] F. R. Fan, Z. Q. Tian, Z. L. Wang, *Nano Energy* **2012**, *1*, 328.
[4] D. Liu, Y. Gao, L. Zhou, J. Wang, Z. L. Wang, *Nano Res.* **2023**, *16*, 22698.
[5] Y. Yu, H. Li, D. Zhao, Q. Gao, X. Li, J. Wang, Z. L. Wang, T. Cheng, *Mater. Today* **2023**, *64*, 61.
[6] A. Chen, C. Zhang, G. Zhu, Z. L. Wang, *Adv. Sci.* **2020**, *7*, 2000186.
[7] a) Z. Shao, J. Chen, Q. Xie, L. Mi, *Coord. Chem. Rev.* **2023**, *486*, 215118; b) P. K. Nitha, A. Chandrasekhar, *Mater. Today Energy* **2023**, *37*, 101393.
[8] a) L. Zhai, W. Wei, B. Ma, W. Ye, J. Wang, W. Chen, X. Yang, S. Cui, Z. Wu, C. Soutis, G. Zhu, L. Mi, *ACS Materials Lett* **2020**, *2*, 1691; b) L. Zhai, S. Cui, B. Tong, W. Chen, Z. Wu, C. Soutis, D. Jiang, G. Zhu, L. Mi, *Chem. Eur. J.* **2020**, *26*, 5784; c) C. Lin, L. Sun, X. Meng, X. Yuan, C. X. Cui, H. Qiao, P. Chen, S. Cui, L. Zhai, L. Mi, *Angew. Chem., Int. Ed.* **2022**, *61*, e202211601; d) S. Yao, M. Zheng, S. Wang, T. Huang, Z. Wang, Y. Zhao, W. Yuan, Z. Li, Z. L. Wang, L. Li, *Adv. Funct. Mater.* **2022**, *32*, 2209142; e) S. Hajra, J. Panda, J. Swain, H. G. Kim, M. Sahu, M. K. Rana, R. Samantaray, H. J. Kim, R. Sahu, *Nano Energy* **2022**, *101*, 107620; f) L. Shi, V. S. Kale, Z. Tian, X. Xu, Y. Lei, S. Kandambeth, Y. Wang, P. T. Parvatkar, O. Shekhah, M. Eddaoudi, H. N. Alshareef, *Adv. Funct. Mater.* **2023**, *33*, 2212891; g) N. Meng, Y. Zhang, W. Liu, Q. Chen, N. Soykeabkaew, Y. Liao, *Adv. Funct. Mater.* **2024**, *34*, 2313534.
[9] a) G. Khandelwal, A. Chandrasekhar, N. P. M. J. Raj, S. J. Kim, *Adv. Energy Mater.* **2019**, *9*, 1803581; b) Y. Guo, Y. Cao, Z. Chen, R. Li, W. Gong, W. Yang, Q. Zhang, H. Wang, *Nano Energy* **2020**, *70*, 104517; c) G. Khandelwal, N. P. M. J. Raj, S. J. Kim, *J. Mater. Chem. A* **2020**, *8*, 17817; d) S. Hajra, M. Sahu, A. M. Padhan, I. S. Lee, D. K. Yi, P. Alagarsamy, S. S. Nanda, H. J. Kim, *Adv. Funct. Mater.* **2021**, *31*, 2101829; e) C. Huang, G. Lu, N. Qin, Z. Shao, D. Zhang, C. Soutis, Y. Y. Zhang, L. Mi, H. Hou, *ACS Appl. Mater. Interfaces* **2022**, *14*, 16424; f) R. A. Shaukat, Q. M. Saqib, J. Kim, H. Song, M. U. Khan, M. Y. Chougale, J. Bae, M. J. Choi, *Nano Energy* **2022**, *96*, 107128; g) Z. Chen, Y. Cao, W. Yang, L. An, H. Fan, Y. Guo, *J. Mater. Chem. A* **2022**, *10*, 799; h) Q. Xi, Z. Chen, Y. Li, F. Liu, Y. Guo, *A. C. S. Appl. Electron. Mater.* **2023**, *5*, 5215.
[10] J. S. M. Lee, A. I. Cooper, *Chem. Rev.* **2020**, *120*, 2171.
[11] S. I. Park, D. M. Lee, C. W. Kang, S. M. Lee, H. J. Kim, Y. J. Ko, S. W. Kim, S. U. Son, *J. Mater. Chem. A* **2021**, *9*, 12560.
[12] a) C. W. Kang, D. M. Lee, J. Park, S. Bang, S. W. Kim, S. U. Son, *Angew. Chem., Int. Ed.* **2022**, *61*, e202209659; b) K. Ghosh, C. Iffelsberger, M. Konečny, J. Vyskočil, J. Michalička, M. Pumera, *Adv. Energy Mater.* **2023**, *13*, 2203476.
[13] X. Lang, A. Hirata, T. Fujita, M. Chen, *Nat. Nanotechnol.* **2011**, *6*, 232.
[14] a) J. Wang, D. Zhang, F. Nie, R. Zhang, X. Fang, Y. Wang, *Environ. Sci. Pollut. Res.* **2023**, *30*, 15377; b) H. Zhang, A. Wu, H. Fu, L. Zhang, H. Liu, S. Zheng, H. Wan, Z. Xu, *R. S. C. Adv.* **2017**, *7*, 41228.
[15] a) J. C. Villegas, L. J. Garces, S. Gomez, J. P. Durand, S. L. Suib, *Chem. Mater.* **2005**, *17*, 1910; b) A. S. Poyraz, J. Laughlin, Z. Zec, *Electrochim. Acta* **2019**, *305*, 423.
[16] R. A. Davoglio, G. Cabello, J. F. Marco, S. R. Biaggio, *Electrochim. Acta* **2018**, *261*, 428.
[17] K. Cho, C. W. Kang, S. H. Ryu, J. Y. Jang, S. U. Son, *J. Mater. Chem. A* **2022**, *10*, 6950.
[18] H. Chen, Y. Wang, Y. K. Lv, *R. S. C. Adv.* **2016**, *6*, 54032.
[19] J. H. Ko, S. M. Lee, H. J. Kim, Y. J. Ko, S. U. Son, *ACS Macro Lett.* **2018**, *7*, 1353.
[20] J. Y. Jang, G. H. Kim, Y. J. Ko, K. C. Ko, S. U. Son, *Polym. Chem.* **2023**, *14*, 2958.
[21] L. Khandare, S. Terdale, *Appl. Surf. Sci.* **2017**, *418*, 22.
[22] Q. Tang, Y. Z. Fan, L. Han, Y. Z. Yang, N. B. Li, H. Q. Luo, *Microchim. Acta* **2020**, *187*, 475.

[23] G. Xie, X. Liu, Q. Li, H. Lin, Y. Li, M. Nie, L. Qin, *J. Mater. Sci.* **2017**, *52*, 10915.
[24] G. P. Lopez, D. G. Castner, B. D. Ratner, *Surf. Interface Anal.* **1991**, *17*, 267.
[25] M. A. F. Basha, *Polymer J.* **2010**, *42*, 728.
[26] W. H. Eisa, E. Al-Ashkar, S. M. El-Mossalamy, S. S. M. Ali, *Chem. Phys. Lett.* **2016**, *651*, 28.
[27] J. Kim, H. Ryu, S. M. Kim, H. Y. Lee, A. Karami, D. Galayko, D. Kang, S. S. Kwak, H. J. Yoon, P. Basset, S. W. Kim, *Adv. Mater. Technol.* **2024**, *9*, 2301309.
[28] Z. L. Wang, *ACS Nano* **2013**, *7*, 9533.
[29] A. P. O'Mullane, N. Fay, A. Nafady, A. M. Bond, *J. Am. Chem. Soc.* **2007**, *129*, 2066.
[30] M. Horn, H. Mayr, *J. Phys. Org. Chem.* **2012**, *25*, 979.